Nano Research

Open Access

Research Article

Facet-dependent dual active sites of CeO_2 govern distinct adsorption mechanisms for fluorinated organics and inorganic fluoride

Youmei Xu[1], Beizhao Chen[1,2], Aling Wan[1], Weiwen Chen[1], Chaoqun Zhu[1], Shidong Zheng[1], Zhipeng Liu[1], and Zhongying Wang[1,3] ✉

[1] School of Environmental Science and Engineering, Southern University of Science and Technology, Shenzhen 518055, China
[2] Department of Civil and Environmental Engineering, The Hong Kong Polytechnic University, Hung Hom, Kowloon, Hong Kong, China
[3] Guangdong Provincial Key Laboratory of Soil and Groundwater Pollution Control, Southern University of Science and Technology, Shenzhen 518055, China

Cite this article: *Nano Research*, **2026**, *19*, 94908404. https://doi.org/10.26599/NR.2026.94908404

ABSTRACT: Understanding how crystal facets dictate the adsorption mechanisms of multifunctional oxides is crucial for designing selective materials for fluorine-containing contaminants. Here, CeO_2 nanocrystals with dominant (111) facets in octahedra (Oct), (110) facets in rods (Rod), and (100) facets in cubes (Cube) were synthesized to elucidate facet-dependent interactions with fluorinated organics and inorganic fluoride. Oct exhibited the highest capacity and kinetics for perfluorooctanoic acid (PFOA) adsorption, while Rod showed superior performance toward F^-. Spectroscopic analyses and site-quenching tests revealed distinct active sites: surface hydroxyl groups and oxygen vacancies governed F^- uptake via ion exchange and vacancy filling, whereas unsaturated Ce(IV) Lewis acid sites drove PFOA adsorption through C–F bond polarization and lattice oxygen substitution. Pyridine-IR and phosphate inhibition experiments confirmed the key role of facet-dependent Lewis acidity, following the order Oct > Rod > Cube. DFT calculations further demonstrated that the (110) facet favors hydroxyl and F^- binding, while the (111) facet exhibits the strongest Lewis acidity and charge transfer with fluorinated organics. This study establishes the structure–facet–function correlation in CeO_2, unveiling dual active-site mechanisms that differentiate inorganic and organic fluorine adsorption and offering mechanistic insights for rational design of advanced fluorine-selective materials.

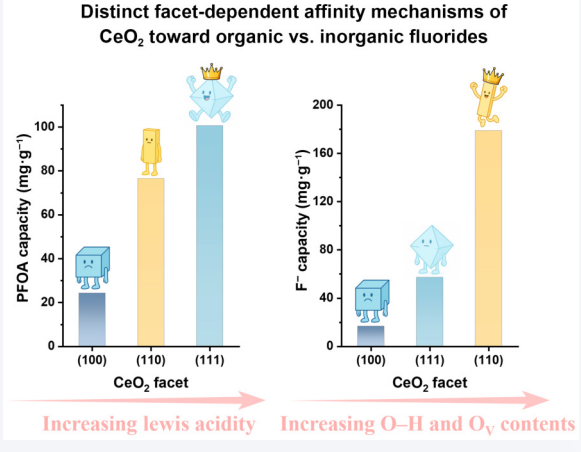

KEYWORDS: facet-engineering, CeO_2, fluorinated compounds, fluoride, adsorption mechanism

1 Introduction

Fluorine-containing contaminants, including inorganic fluoride ions (F^-) and organic per- and polyfluoroalkyl substances (PFAS), are of increasing environmental concern due to their persistence, mobility, and toxicity. Elevated concentrations of F^- from fluorine chemical industry and geogenic sources pose significant risks to public health [1, 2]. Moreover, polyfluorine emissions occurring throughout different stages of fluorine chemical production contribute to the release of various organic fluorine pollutants [3]. Among these, PFAS, high-value products of the fluorochemical industry [4], are particularly concerning due to their widespread use and exceptional stability [5, 6]. Owing to the strong and highly polarized carbon–fluorine (C–F) bond (~ 485 kJ·mol^{-1}) [7], PFAS exhibit outstanding resistance to thermal, chemical, and biological degradation. Consequently, their persistence and global ubiquity have led to their recognition as one of the most challenging classes of emerging environmental contaminants [8].

Conventional physical methods for fluoride removal—such as adsorption, coagulation, and membrane separation—often suffer from poor selectivity and strong dependence on solution chemistry (e.g., pH, competing anions, and natural organic matter) [9–11]. Meanwhile, chemical destruction routes for PFAS, including advanced oxidation/reduction processes [12, 13], electrocatalysis [14, 15], plasma catalysis [16–18], are similarly constrained by the

Received: November 12, 2025; **Revised:** January 4, 2026
Accepted: January 5, 2026

✉Address correspondence to wangzy6@sustech.edu.cn

intrinsically low affinity between conventional catalysts and PFAS molecules. The absence of strong interfacial interactions hampers mass transfer and active-site accessibility, resulting in sluggish reaction kinetics and high energy consumption [8, 19, 20]. These limitations highlight the need for rationally designed materials that possess intrinsic selectivity toward fluorinated species. Such fluorine-affinitive materials can not only serve as efficient adsorbents for both inorganic fluoride and PFAS but also function as catalytic platforms that facilitate the activation and cleavage of strong C–F bonds, offering an integrated strategy for fluorine capture and degradation.

Nanostructured metal oxides have garnered considerable attention for removing fluorine species due to their high surface reactivity, tunable chemistry, and abundance of active sites. Among them, cerium dioxide (CeO_2) stands out as a multifunctional candidate due to its unique redox flexibility and surface coordination environment, characterized by the coexistence of Ce^{3+}/Ce^{4+} pairs, abundant oxygen vacancies, and strong Lewis acidity [21, 22]. These features endow CeO_2 with dual affinity toward fluorine species: the ability to form robust Ce–F bonds facilitates fluoride adsorption, while the same interaction can polarize and weaken the C–F bond in fluorinated organics, thereby promoting its activation and cleavage [21, 23, 24]. Leveraging these attributes, CeO_2-based materials have shown great promise in both adsorption and catalytic degradation applications. For instance, CeO_2–ZrO_2 nanocages achieved high fluoride adsorption capacities up to 175 $mg·g^{-1}$ [25], while Bi_2O_3/CeO_2 plasma catalysts enabled nearly complete PFOA decomposition within 30 min with a 5.7-fold enhancement in rate and 72.6% reduction in energy consumption compared to plasma alone [26]. Nevertheless, most existing studies address either inorganic fluoride or PFAS separately [27–30], ignoring the frequent coexistence of the two in natural and engineered environments, and the fundamental distinctions in their interfacial affinity and reaction mechanisms on CeO_2 remain largely unexplored, leaving a critical gap in understanding the selective remediation strategies for fluoride pollution by CeO_2-based materials.

Given these unique redox and coordination properties, facet engineering of CeO_2 nanocrystals provides an effective route to further tailor their surface chemistry and reactivity. The low-index (111), (110), and (100) planes of CeO_2 are well known to expose distinct coordination environments, oxygen vacancy formation energies, hydroxylation tendencies, and redox behaviors [31, 32]. By selectively tuning these surface terminations, facet engineering not only enhances performance but also reveals the structure–activity relationships that govern interfacial reactions [33]. For example, Tan et al. found that CeO_2 nanocrystals dominated by the (111) facet exhibited superior dephosphorylation activity, with reactivity closely associated with Ce oxidation states and surface acidity [34]. Through systematic facet engineering, it becomes possible to distinguish the affinity mechanisms of CeO_2 toward F^- and PFAS, thereby identifying the key active sites and surface factors that dictate their respective interactions. However, the specific mechanisms by which CeO_2 facets regulate their affinity and activation toward different fluorine species remain largely unexplored. Addressing this gap is essential for identifying facet-dependent active sites that determine selective adsorption and catalytic activation of fluorine-bearing contaminants.

Herein, we systematically investigated, for the first time, how facet-dependent properties of CeO_2 regulate the adsorption of fluorinated organics and inorganic fluoride, thereby disentangling their distinct affinity mechanisms on a unified platform. Facet-controlled CeO_2 nanocrystals predominantly exposing the (111), (110), or (100) facets were synthesized, and the corresponding structure–activity relationships were established. By integrating adsorption experiments with density functional theory (DFT) calculations, we revealed that fluorinated organics represented by perfluorooctanoic acid (PFOA) and F^- favor different optimal facets on CeO_2 and are governed by fundamentally distinct adsorption mechanisms and active-site determinants.

2 Materials and methods

2.1 Chemicals

Cerium nitrate hexahydrate ($Ce(NO_3)_3·6H_2O$, 99.95%), perfluorooctanoic acid (PFOA, 96%), perfluorooctanesulfonic acid (PFOS, 99.5%), sodium fluoride (NaF, 99.9%), and activated carbon powders (AC, 400 mesh) were obtained from Macklin, China. Hydrochloric acid (HCl, 37%), sodium hydroxide (NaOH, ≥ 96%), trifluoroacetic acid (TFA, 99%), and sodium phosphate (Na_3PO_4, 96%) were purchased from Aladdin, China. HPLC-grade ammonium acetate (NH_4Ac, ≥ 99%, Macklin, China) and methanol (MeOH, Merck, Germany) were used for mass spectrometry analysis. Ethanol (≥ 99.7%) was obtained from Sinopharm Reagent, China. All reagents used in this work were used without further purification. Ultrapure water (resistivity ≥ 18 MΩ·cm) produced by a Millipore system (Millipore, Billerica, MA, USA) was used to prepare all solutions.

2.2 Preparation of facet-controlled CeO_2

CeO_2 nanocrystals with different exposed facets were synthesized via a hydrothermal method adapted from previously reported literature [35, 36]. Octahedra, nanorods, and nanocubes were prepared using similar procedures, with variations in the dosages of $Ce(NO_3)_3·6H_2O$ and NaOH, and hydrothermal conditions. For CeO_2 octahedra, 1.95 g of $Ce(NO_3)_3·6H_2O$ and 0.08 g of NaOH were dissolved in 40 mL of ultrapure water, stirred at room temperature for 1 h to obtain a homogeneous solution, and then transferred to a 50 mL polytetrafluoroethylene (PTFE) hydrothermal reactor. The mixture was heated at 180 °C for 12 h. After natural cooling, the precipitate was collected by centrifugation, thoroughly washed several times with ultrapure water and ethanol to remove residual impurities, and then dried in a vacuum oven at 60 °C overnight. For CeO_2 nanorods, 1.8 g of $Ce(NO_3)_3·6H_2O$ and 8.4 g of NaOH were used, and the hydrothermal reaction was carried out at 100 °C for 24 h. For CeO_2 nanocubes, 0.5 g of $Ce(NO_3)_3·6H_2O$ and 4.0 g of NaOH were used, followed by hydrothermal treatment at 200 °C for 24 h. The resulting samples were denoted as Oct, Rod, and Cube, respectively. Additionally, to further obtain a series of CeO_2 samples with the same crystal facet but varying chemical states, the powders of Oct, Rod, and Cube were calcined in air at 200, 400, 600, and 800 °C for 4 h with a heating rate of 10 $°C·min^{-1}$. These calcined products were labeled as O-, R-, and C-200/400/600/800, respectively.

2.3 Characterization

Transmission electron microscopy (TEM; Talos F200X G2, Thermo Fisher Scientific, USA) coupled with an energy-dispersive spectroscope (EDS) was employed to observe the morphology,

surface element distribution, and exposed facet of CeO_2 nanocrystals. The chemical composition and crystalline nature of CeO_2 were explored by powder X-ray diffraction (XRD; Rigaku Smartlab 9 kW, Rigaku, Japan), operated at 45 kV and 200 mA with Cu-Kα radiation (λ = 1.5406 Å). Nitrogen adsorption-desorption isotherms were measured using the Brunauer–Emmet–Teller (BET) method (ASAP 2020, Micromeritics, USA) in a liquid N_2 bath (77 K) to determine the specific surface area and pore size of CeO_2. Before the measurements, the samples were degassed at 200 °C for 6 h, under a pressure below 5 Pa. The surface zeta potential of CeO_2 was measured using a Zetasizer Nano ZS instrument (NanoBrook Omini, Brookhaven, USA). Fourier-transform infrared spectroscopy (FT-IR; Vertex 70v, Bruker, Germany) was employed to identify the characteristic functional groups of CeO_2. Raman spectra were collected using a LabRAM HR Evolution with a 532 nm laser (Horiba, Japan). X-ray photoelectron spectroscopy (XPS; PHI 5000 Versaprobe III, ULVAC-PHI, Japan) was employed to determine the elemental compositions and chemical states of CeO_2, with binding energies calibrated to the C 1s peak at 284.8 eV. To characterize the Lewis acidity of CeO_2, pyridine-IR spectra were collected using a Tensor 27 spectrometer (Bruker, Germany). Prior to measurements, the samples were pretreated under vacuum at 200 °C for 1 h, exposed to pyridine vapor at room temperature for 0.5 h, and subsequently heated to 150 °C and evacuated for 1 h to desorb physically adsorbed pyridine [37].

2.4 Adsorption experiments

Fluorinated organic and inorganic fluoride stock solutions were prepared using ultrapure water, with PFOA (1 mg·L^{-1}) and NaF (50 mg·L^{-1} for F^-), and the pH was adjusted to 3.5 with 1 M HCl. Batch adsorption experiments were conducted to evaluate the adsorption performances of CeO_2 materials. In each experiment, 20 mg of adsorbent was added to 40 mL of the test solution (PFOA or F^-) in 50 mL polypropylene (PP) vials, which were stirred at 400 rpm at room temperature (25 ± 1 °C) to ensure homogeneous mixing. After equilibration, the suspensions were filtered through 0.22 μm polyethersulfone (PES) syringe filters (Tianjin Jinteng Technology Co., Ltd.) for subsequent analysis. Residual PFOA and F^- concentrations were determined employing a high-performance liquid chromatograph coupled with a triple quadrupole mass spectrometer (LCMS-8045, Shimadzu, Japan) and ion chromatography (IC; Dionex Aquion RFIC, Thermo Fisher Scientific, USA), respectively. Detailed analytical procedures are provided in Texts S1 and S2 in the Electronic Supplementary Material (ESM).

2.5 DFT calculations

Density functional theory calculations were performed with the Vienna *ab initio* simulation package (VASP) [38]. The exchange–correlation interactions among electrons were treated using the generalized gradient approximation (GGA) with the Perdew–Burke–Ernzerhof (PBE) functional. The CeO_2 (100), (110), and (111) facets, with or without an oxygen vacancy, were modeled using a (3 × 3) supercell containing three atomic layers, corresponding to the formula $Ce_{27}O_{54}$. For vacancy-containing models, one oxygen atom was removed from the surface layer. A 25 Å vacuum layer was added perpendicular to the surface to avoid spurious slab–slab interactions. The Monkhorst–Pack grid of 3 × 3 × 1 was employed for the optimizations and energy calculations. The interactions between ions and valence electrons were described using projector augmented wave (PAW) potentials with a plane-wave cutoff of 400 eV [39]. To properly account for the Coulomb interactions of Ce 4f orbitals, the Hubbard U correction (DFT + U) method was applied with an effective U value of 5.0 eV [40]. Additionally, the DFT + D^3 method was incorporated to correct for long-range dispersion interactions [41]. The optimizations and single-point energy were considered converged once the force threshold reached 0.05 eV·Å^{-1}, and electronic self-consistency iterations converged to 10^{-5} eV.

The adsorption energy (E_{ads}) was calculated according to the following equation

$$E_{ads} = E_{substrate-adsorbate} - E_{substrate} - E_{adsorbate} \quad (1)$$

where $E_{substrate\text{-}adsorbate}$, $E_{adsorbate}$, and $E_{substrate}$ are the total energies of substrate-adsorbate (F^--CeO_2, OH-CeO_2, PFOA-CeO_2), adsorbate (F^-, O–H, PFOA), and CeO_2, respectively.

Charge density difference (CDD) analysis was applied to reveal the activation effects between cerium sites and C–F bonds. The CDD was calculated according to the equation

$$\rho = \rho_{substrate-adsorbate} - \rho_{substrate} - \rho_{adsorbate} \quad (2)$$

where $\rho_{substrate\text{-}adsorbate}$, $\rho_{substrate}$, and $\rho_{adsorbate}$ represent the electron densities of PFOA-CeO_2, PFOA, and CeO_2, respectively. The charge densities were visualized using the VESTA software [42].

3 Results and discussion

3.1 CeO_2 synthesis and characterization

Three types of CeO_2 with distinct dominant exposed crystal facets were successfully synthesized by adjusting the precursor concentrations and hydrothermal conditions to direct preferential crystal growth [43]. As shown in Figs. 1(a)–1(f), TEM and HRTEM analyses revealed the distinct morphologies and lattice structures of the three samples. Specifically, Oct displayed well-defined octahedra with an average size of ~ 10 nm (Fig. 1(a)). The HRTEM image (Fig. 1(b)) revealed the interplanar spacing of 0.31 nm, corresponding to the (111) facet of CeO_2 [44]. Figure 1(c) showed a clear rod-like morphology, with an average length of 70–100 nm and a diameter of 5–8 nm. The observed interplanar spacings of 0.27 and 0.19 nm were assigned to the (100) and (110) facets (Fig. 1(d)). Notably, previous studies have demonstrated that the (110) plane is the most thermodynamically stable and extensively exposed surface in rod-like CeO_2 [45], suggesting that the Rod sample predominantly exposes the (110) facet. The cubic-shaped CeO_2 exhibited sizes of 80–120 nm with an interplanar spacing of 0.27 nm attributed to the (100) facet (Figs. 1(e) and 1(f)). Figure 1(g) presents the XRD patterns of the three CeO_2 samples, all of which can be indexed to the face-centered cubic fluorite structure of CeO_2 (space group $Fm\bar{3}m$, PDF#34-0394) [46], without detectable impurity peaks, confirming their high crystalline purity. The diffraction peak intensities and full width at half maximum (FWHM) varied among Oct, Rod, and Cube, reflecting differences in crystallinity. Sharper and stronger peaks generally indicate higher crystallinity, suggesting the order: Cube > Oct > Rod. This implies that Rod may possess a higher density of structural defects [47].

Nitrogen adsorption–desorption isotherms (Fig. S1 in the ESM)

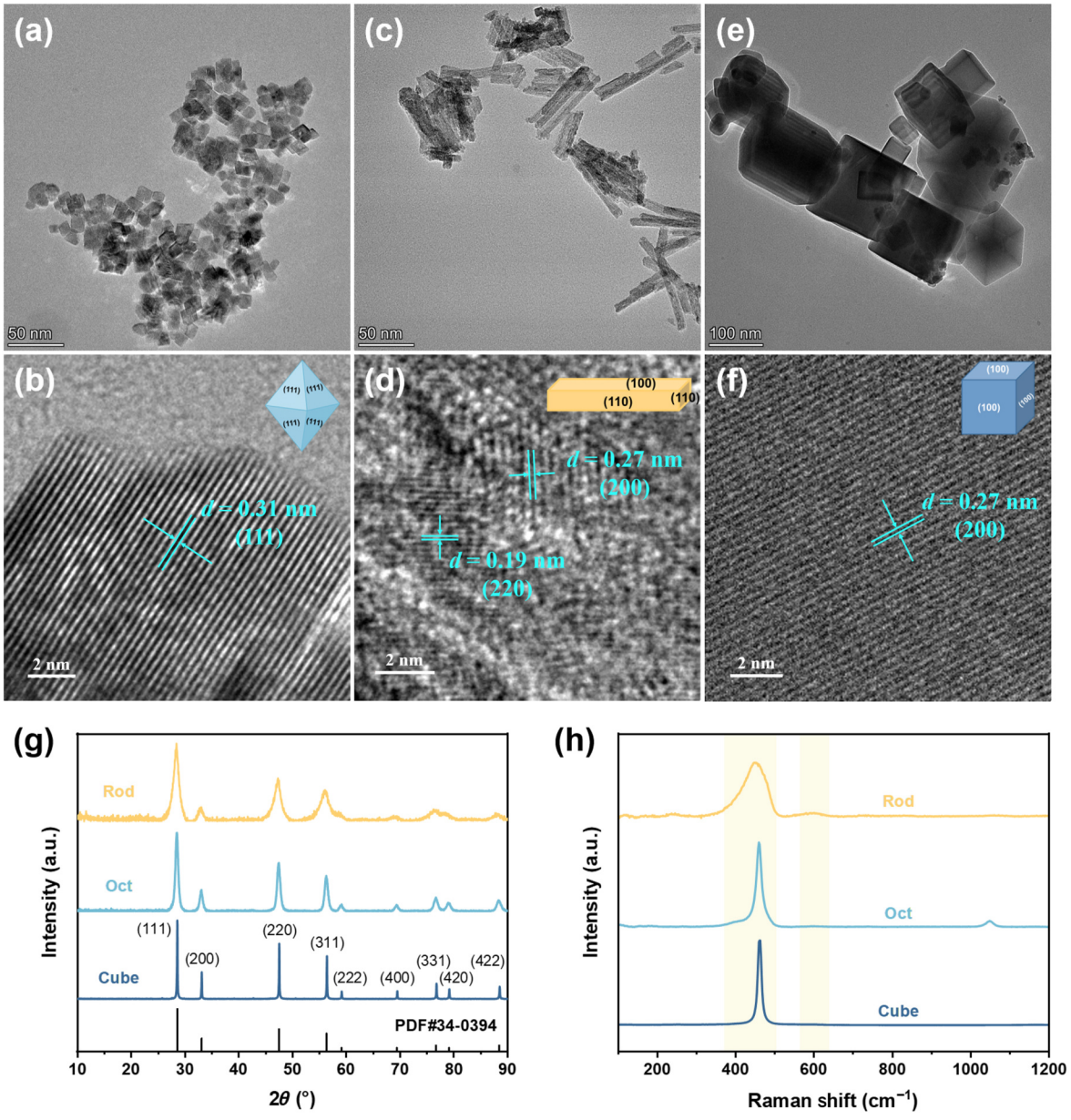

Figure 1 Characterizations of CeO_2: TEM and HRTEM images of ((a) and (b)) Oct, ((c) and (d)) Rod, and ((e) and (f)) Cube; (g) XRD patterns; and (h) Raman spectra.

further revealed that all samples displayed type IV isotherms with H3-type hysteresis loops, characteristic of mesoporous materials [48]. The specific surface area and pore volume of the three CeO_2 are summarized in Table S1 in the ESM. Among the three, Rod showed the highest specific surface area and pore volume (88.46 $m^2 \cdot g^{-1}$, 0.32 $cm^3 \cdot g^{-1}$), followed by Oct (67.96 $m^2 \cdot g^{-1}$, 0.13 $cm^3 \cdot g^{-1}$) and Cube (22.85 $m^2 \cdot g^{-1}$, 0.08 $cm^3 \cdot g^{-1}$), which aligned with the morphological differences observed in the TEM images. Zeta potential measurements (Fig. S2 in the ESM) revealed that Oct exhibited the highest isoelectric point (IEP), indicating a broader pH range with positive surface charge and thus stronger electrostatic attraction toward negatively charged pollutants.

Raman spectroscopy was employed to probe the defect structures of the CeO_2 nanocrystals (Fig. 1(h)). The strong peak located at approximately 462 cm^{-1} corresponds to the F_{2g} symmetry vibrational mode of the fluorite structure, while the broadband at around 598 cm^{-1} is attributed to the defect-induced modes (D-band). The intensity ratio (I_D/I_{F2g}) is commonly used to evaluate oxygen defects in CeO_2 [49]. Among the samples, Rod exhibited the highest I_D/I_{F2g} ratio of 0.18, followed by Oct (0.031) and Cube (0.014), indicating that Rod possessed the greatest concentration of intrinsic defects, consistent with the XRD results. Overall, the CeO_2 nanocrystals exhibited facet-dependent structural and surface characteristics—defect-rich (110) Rod, electropositive (111) Oct, and highly crystalline (100) Cube—features that are expected to govern their interfacial reactivity and adsorption selectivity.

3.2 Adsorption performance of CeO_2 for PFOA and F^-

To gain insights into facet-dependent performance of CeO_2 for PFOA and F^-, batch adsorption experiments were conducted at pH ~ 3.5, where the zeta potentials of the three CeO_2 samples were comparable, thereby minimizing electrostatic effects. As shown in Fig. 2(a), Oct, Rod, and Cube exhibited rapid PFOA removal with efficiencies of 100%, 94.4%, and 75.6% within 24 h, respectively,

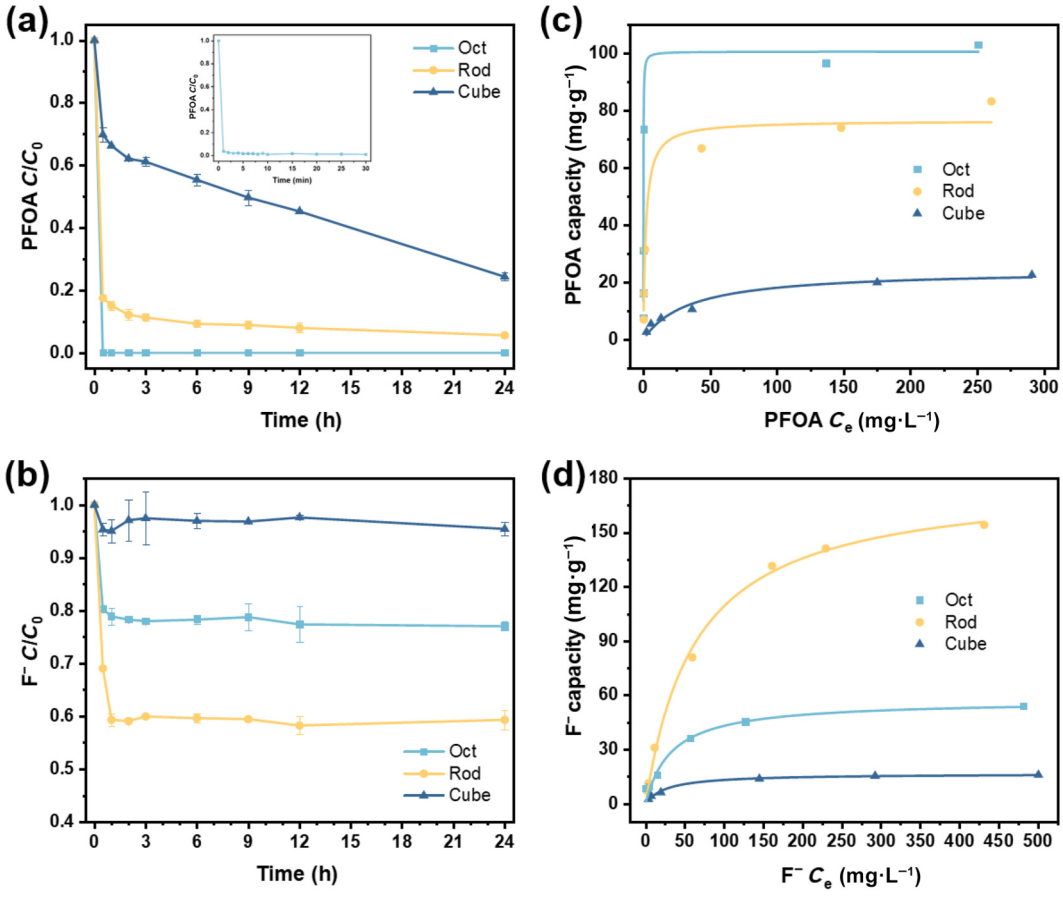

Figure 2 Adsorption performance of CeO_2 for PFOA and F^-: kinetic curves for (a) PFOA and (b) F^- adsorption ([PFOA] = 1 mg·L^{-1}, [F^-] = 50 mg·L^{-1}, pH ~ 3.5, CeO_2 dosage = 0.5 g·L^{-1}); adsorption isotherms of (c) PFOA and (d) F^- on CeO_2 ([PFOA] = 1–300 mg·L^{-1}, [F^-] = 5–500 mg·L^{-1}, pH ~ 3.5, CeO_2 dosage = 0.5 g·L^{-1}).

demonstrating a pronounced facet dependence. Kinetic data were better described by the pseudo-second-order model than the pseudo-first-order model (Figs. S3(a) and S3(c) and Table S2 in the ESM), suggesting that chemisorption involving valence forces through the electron sharing or exchange was the rate-limiting step [50]. The rate constant of Oct (26.81 g·mg^{-1}·h^{-1}) far exceeded those of Rod (1.66 g·mg^{-1}·h^{-1}) and Cube (0.49 g·mg^{-1}·h^{-1}), consistent with its superior removal efficiency. Langmuir isotherm fitting confirmed monolayer adsorption of PFOA by CeO_2 (Fig. 2(c)), and TEM-EDS mapping images verified uniform distribution of PFOA on the CeO_2 surface (Fig. S4(a) in the ESM). The maximum adsorption capacities of Oct, Rod, and Cube for PFOA were 100.6, 76.5, and 24.3 mg·g^{-1}, respectively (Table S3 in the ESM). Overall, Oct with a dominant (111) facet exhibited both the highest adsorption capacity and the fastest kinetics, confirming it as the most effective CeO_2 structure for PFOA removal.

A similar trend was observed for trifluoroacetic acid (TFA), a highly hydrophilic and mobile organic fluoride [51]. Oct achieved 52% TFA removal, far exceeding Rod (11.9%), Cube (6.9%), and activated carbon (11.9%) (Fig. S5(a) in the ESM). Unlike activated carbon, which primarily relies on hydrophobic interactions and thus fails to effectively capture small, water-soluble molecules [52], Oct demonstrated strong affinity even toward such highly hydrophilic fluorinated species. Furthermore, Oct also achieved 100% removal efficiency of perfluorooctanesulfonic acid (PFOS), a sulfonate-terminated organic fluoride, followed by Rod (80.3%) and Cube (39.2%) (Fig. S5(b) in the ESM). Combined with its nearly complete removal of the more hydrophobic carboxylate PFOA, these findings highlight Oct's exceptional adsorption performance and broad applicability across organic fluorides with differing hydrophobicity and terminal groups, underscoring its facet-dependent reactivity.

In contrast, the adsorption behavior toward F^- differed markedly (Fig. 2(b) and Fig. S6 in the ESM). Rod showed the highest removal efficiency, reaching 40.6%, followed by Oct (22.9%) and Cube (4.6%). All adsorption data for F^- were well described by the Langmuir model (Fig. 2(d)), indicating monolayer adsorption on homogeneous surface sites (Fig. S4(b) in the ESM) [53]. The maximum adsorption capacities were determined to be 178.9, 57.2, and 16.7 mg·g^{-1} for Rod, Oct, and Cube, respectively (Table S3 in the ESM), and the corresponding kinetic constants followed the same trend (0.79, 0.45, and 0.37 g·mg^{-1}·h^{-1}; Table S2 in the ESM). A notable phenomenon during F^- adsorption was the increase in solution pH (Table S4 in the ESM). For Rod, the final pH rose by 3.7 units to 7.2, and the extent of this increase correlated positively with F^- removal efficiency across the three samples. In contrast, the pH of the PFOA solution remained essentially unchanged, further underscoring distinct adsorption mechanisms governing CeO_2 interactions with inorganic and organic fluorine species.

The regeneration stability of Oct for PFOA and Rod for F^- was evaluated with five adsorption–desorption cycles. Oct after adsorbing PFOA was regenerated using 0.1 M NaOH in MeOH, whereas F^--loaded Rod was regenerated by 0.1 M NaOH [54, 55], and the corresponding desorption efficiencies were 100% and

96.3%, respectively. As shown in Fig. S7 in the ESM, Oct and Rod both retained stable and high adsorption performances over five cycles, further demonstrating their superior recyclability and applicability.

Overall, the three CeO_2 nanocrystals exhibited facet-dependent adsorption behaviors. For PFOA, the removal efficiency followed the order Oct > Rod > Cube, whereas for F^- it followed Rod > Oct > Cube. Notably, even in mixed system containing both PFOA and F^-, Oct and Rod remained the most effective adsorbents for PFOA and F^-, respectively, exhibiting pronounced facet-dependent selectivity (Fig. S8 in the ESM). To decouple the influence of surface area, adsorption experiments were normalized by adjusting adsorbent dosages according to specific surface areas [56]. Even under equal surface area conditions (Fig. S9 in the ESM), the same performance trends were maintained for both PFOA (Oct > Rod > Cube) and F^- (Rod > Oct > Cube), with area-normalized removal densities of 0.029, 0.026 and 0.0067 $mg_{PFOA}·m^{-2}$ for Oct, Rod, and Cube, and 0.46, 0.29 and 0.22 $mg_{F^-}·m^{-2}$ for Rod, Oct, and Cube, respectively. These results confirm that while surface area contributes to adsorption, the dominant factor is the exposed crystal facets and their associated surface chemistry.

3.3 Facet-dependent mechanisms governing CeO_2 adsorption

To explore the facet-dependent mechanisms of CeO_2 for PFOA and F^-, the post-adsorption samples (denoted as O–, R–, C–PFOA and O–, R–, C–F, respectively) were characterized by FT-IR and compared with the pristine CeO_2 samples. As shown in Fig. 3(a), a broad O–H stretching band at ~ 3500 cm^{-1} was observed in the pristine samples, with intensity decreasing in the order Rod > Oct > Cube, indicating that Rod possessed the most abundant surface hydroxyl groups. After F^- adsorption, the O–H bands of the O–, R–, and C–F samples were significantly diminished relative to the pristine samples, suggesting an ion-exchange process in which F^- replaced surface O–H groups [57]. This interpretation is consistent with the substantial pH increase observed during F^- adsorption, particularly in the case of Rod (Table S4 in the ESM).

To further verify these observations, XPS was employed to semi-quantitatively characterize surface chemistry changes, particularly variations in hydroxyl and oxygen vacancy contents. The Ce 3d spectra (Fig. 3(b)) exhibited characteristic Ce(IV) peaks at 900.9, 907.1, and 916.8 eV, along with their spin–orbit counterparts at 882.4, 888.8, and 898.3 eV. The peaks at 884.5 and 903.1 eV were associated with Ce(III) $3d_{5/2}$ and Ce(III) $3d_{3/2}$ [58]. The relative Ce(III) content decreased in the order of Rod (19.5%), Oct (13.1%), and Cube (12.2%), indicating that Rod possessed the highest concentration of oxygen vacancies (O_V), as Ce(III) is closely associated with O_V formation [59]. The O 1s spectra (Fig. 3(c)) were deconvoluted into lattice oxygen (O_{latt}, 529.2 eV), chemisorbed oxygen (O_{ads}, 530.9 eV), and hydroxyl oxygen ($O_{O–H}$, 532.6 eV). A higher O_{ads} fraction is generally associated with a greater abundance of oxygen vacancies [60]. Rod exhibited the highest O_{ads} content of 59.4%, significantly exceeding that of Oct (24.2%) and Cube (21.8%), revealing that Rod has more O_V content, consistent with the Raman and Ce 3d XPS spectra results. Meanwhile, the contents of $O_{O–H}$ followed the same trend: Rod (14.3%) > Oct (12.2%) > Cube (6.0%), further demonstrating that Rod contained the most abundant surface hydroxyl groups.

Comparison of high-resolution Ce 3d (Fig. 3(b) and Table S5 in the ESM) and O 1s (Fig. 3(c) and Table S6 in the ESM) spectra before and after adsorption revealed that F^- uptake led to a decrease in the contents of Ce(III), O_{ads} (O_V), and $O_{O–H}$ across all three CeO_2 samples. The most pronounced reductions occurred for Rod, with decreases of 5.9%, 29.6%, and 6.3% in Ce(III), O_{ads} (O_V), and $O_{O–H}$, respectively. The decline in $O_{O–H}$ further supports an ion-exchange mechanism between O–H and F^-, while the simultaneous reduction in O_V and Ce(III) contents suggests that F^- entered the oxygen-vacancy sites and complexed with Ce(III). Owing to the strong

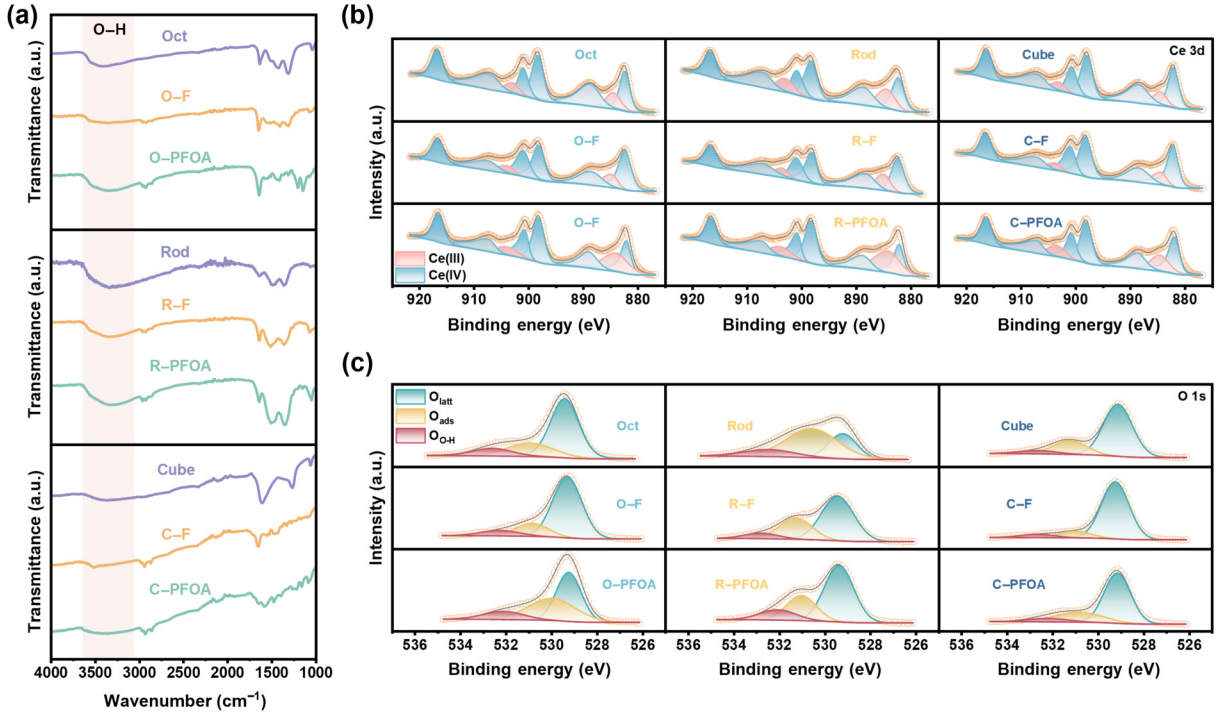

Figure 3 Characterizations of CeO_2 after PFOA and F^- adsorption: (a) FT-IR spectra; HRXPS of (b) Ce 3d and (c) O 1s ([PFOA] = 1 $mg·L^{-1}$, [F^-] = 50 $mg·L^{-1}$, pH ~ 3.5, CeO_2 dosage = 0.5 $g·L^{-1}$).

electronegativity of F^-, electrons withdrawn from Ce(III) likely resulted in its partial oxidation to Ce(IV).

After PFOA adsorption, in contrast to F^-, both Ce(III) and O_V contents increased, with Oct showing the largest rises of 9.6% and 16.4%, respectively (Figs. 3(b) and 3(c), and Tables S5 and S6 in the ESM). This suggests that fluorine atoms in PFOA may substitute lattice oxygen, generating new oxygen vacancies and releasing electrons that subsequently reduce Ce(IV) to Ce(III) [55]. Given that unsaturated Ce(IV) sites act as Lewis acid sites capable of polarizing and activating C–F bonds [34, 61], the observed Ce(IV) reduction provides strong evidence that PFOA adsorption involves Lewis acid–base interactions at Ce(IV) sites. Taken together, these results indicate distinct mechanisms: Inorganic F^- preferentially interacts with Ce(III) and surface O–H groups via ion exchange and vacancy filling, whereas organic PFOA binds more strongly to unsaturated Ce(IV) Lewis acid sites, accompanied by lattice oxygen substitution and Ce(IV) reduction.

To verify that CeO_2 adsorbs PFOA and inorganic fluorides through different active sites and mechanisms, site-quenching experiments were conducted by (i) annealing to eliminate surface O–H groups and oxygen vacancies, and (ii) phosphate addition to block Lewis acid sites. The three CeO_2 samples were calcined at 200, 400, 600, and 800 °C to obtain O-, R-, and C-200/400/600/800, thereby tuning their O–H and O_V contents. As shown in Figs. S10–S13 and Tables S7 and S8 in the ESM, increasing calcination temperature enhanced crystallinity but simultaneously reduced O–H, Ce(III), and O_V contents. Correspondingly, F^- adsorption performance decreased with rising calcination temperature (Fig. 4(a)), and the extent of pH increase followed the same trend (Table S9 in the ESM), both showing a positive correlation with the initial O–H content. This diminishing trend was most pronounced in the Rod group. According to semi-quantitative XPS analysis (Table S8 in the ESM), R-800 exhibited the most significant quenching effect compared with the uncalcined Rod, with a 33.5% reduction in F^- removal. Its O–H and O_V contents also decreased substantially by 8.7% and 34.5%, respectively. Furthermore, the solution pH remained nearly unchanged after reaction with R-800, suggesting that almost no ion exchange occurred. In contrast, calcination had little influence on PFOA adsorption (Fig. 4(b)). Interestingly, for Cube, PFOA uptake even improved after calcination up to 600 °C, possibly due to the exposure of more accessible Lewis acid sites as surface hydroxyl groups and vacancies were diminished (Figs. S10–S13, and Tables S7 and S8 in the ESM). To further exclude changes in specific surface area as a confounding factor, O-, R-, and C-400 were characterized by BET analysis. As shown in Fig. S14 and Table S10 in the ESM, the surface areas of R-400 and C-400 were comparable with those of the corresponding uncalcined samples, and the surface area of O-400 even increased to 122.04 $m^2 \cdot g^{-1}$. Nevertheless, F^- removal efficiencies of the samples calcinated at 400 °C still decreased significantly, confirming that specific surface area was not the dominant factor responsible for the observed inhibition.

To further confirm the critical role of Lewis acid sites in PFOA adsorption, phosphate (PO_4^{3-}), a strong Lewis base, was introduced to competitively block the interactions between CeO_2 Lewis acid sites and PFOA [62]. As shown in Fig. 4(c), the PFOA removal efficiencies of Oct, Rod, and Cube were significantly inhibited in the presence of PO_4^{3-}, whereas F^- adsorption remained largely

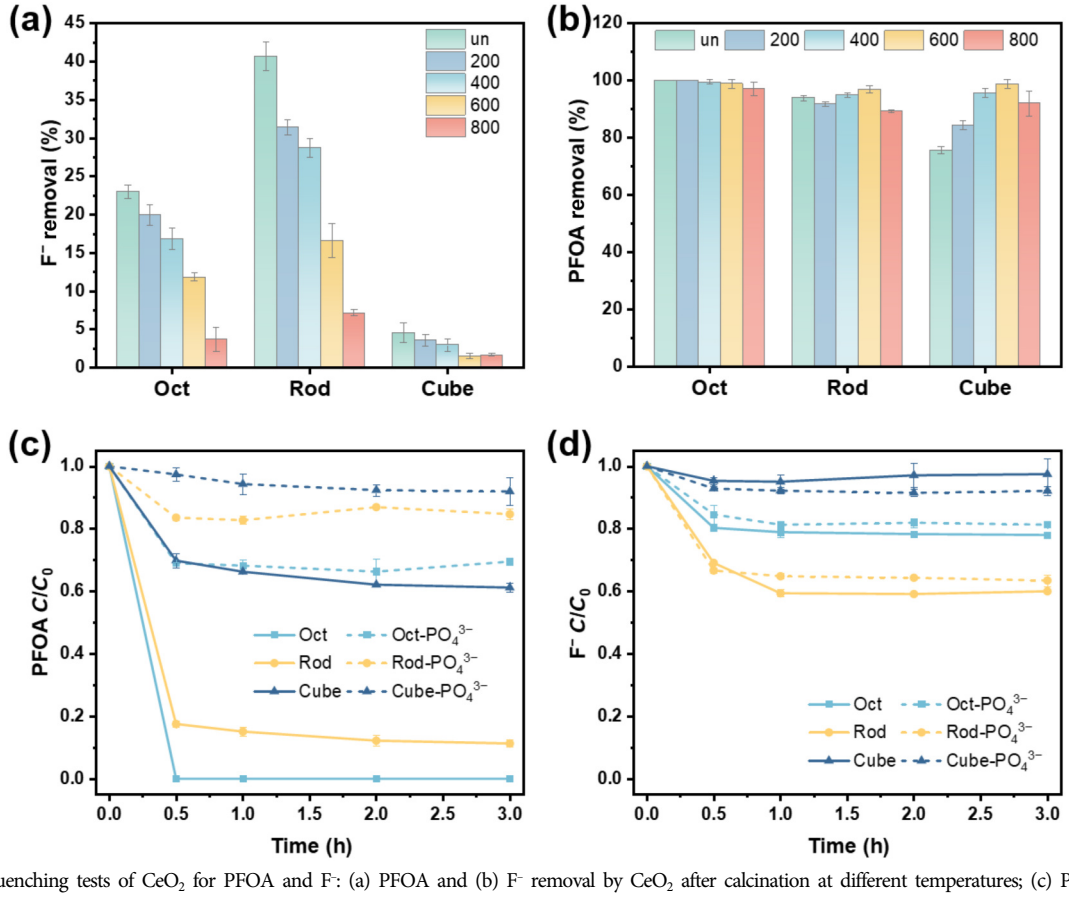

Figure 4 Site-quenching tests of CeO_2 for PFOA and F^-: (a) PFOA and (b) F^- removal by CeO_2 after calcination at different temperatures; (c) PFOA and (d) F^- adsorption kinetic curves in the presence of PO_4^{3-} ([PFOA] = 1 $mg \cdot L^{-1}$, [F^-] = 50 $mg \cdot L^{-1}$, [PO_4^{3-}] = 10 $mg \cdot L^{-1}$, pH ~ 3.5, CeO_2 dosage = 0.5 $g \cdot L^{-1}$).

unaffected (Fig. 4(d)). Additionally, PO_4^{3-} itself exhibited strong and facet-dependent uptake on CeO_2 in the PFOA system, with Oct and Rod achieving > 95% removal, far exceeding that of Cube (39.3%), supporting effective occupation of Lewis acid sites by PO_4^{3-} and the consequent inhibition of PFOA adsorption (Fig. S15 in the ESM). Notably, PO_4^{3-} removal efficiency in the PFOA system was higher than that in the F^- system, likely because PO_4^{3-} can occupy both Lewis acid sites and ion-exchange-related sites in the PFOA system, whereas in the F^- system, it should compete with F^- for available surface sites. The consistently high PO_4^{3-} removal by Rod in both systems further suggests that its performance is strongly supported by abundant ion-exchange sites. Moreover, increasing PO_4^{3-} concentration progressively suppressed PFOA uptake by Oct, but the inhibition effect plateaued at 20–30 mg·L^{-1}, likely due to saturation of accessible surface sites by PO_4^{3-} (Fig. S16 in the ESM). Collectively, these results provide direct evidence that Lewis acid sites govern the affinity of CeO_2 toward organic fluorine species, in sharp contrast to the hydroxyl/O_V-controlled mechanisms dominating F^- uptake.

Building on this understanding, the facet-dependent Lewis acidity of CeO_2 was examined, as variations in the strength of unsaturated Ce(IV) sites—where PFOA primarily interacts—are expected to govern the observed differences in adsorption performance. Pyridine-IR spectra were employed to experimentally quantify Lewis acidity (Text S5 in the ESM). This method relies on the coordination of pyridine molecules with surface Lewis acid sites (electron acceptors such as Ce^{4+}), producing characteristic absorption bands [37]. As shown in Fig. S17(a) in the ESM, the band at ~ 1450 cm^{-1} was assigned to Lewis-coordinated pyridine, while those at ~ 1540 and 1490 cm^{-1} corresponded to Brønsted- and mixed Lewis/Brønsted-coordinated pyridine, respectively [63]. The Lewis acidity of CeO_2, calculated from the integrated absorbance of the 1450 cm^{-1} band, followed the order Oct (81.92 μmol·g^{-1}) > Rod (66.46 μmol·g^{-1}) > Cube (47.77 μmol·g^{-1}), which directly paralleled the order of PFOA adsorption (Fig. S17(a) in the ESM). Moreover, a strong linear correlation (R^2 > 0.97) between Lewis acidity and the Langmuir maximum adsorption capacities for PFOA (Fig. S17(b) in the ESM) further underscores the pivotal role of Lewis acid sites in governing the uptake of organic fluorine species by CeO_2.

Collectively, the spectroscopic analyses and site-quenching experiments provide convergent evidence that CeO_2 interacts with inorganic fluoride and organic fluorine species through distinct adsorption mechanisms (Fig. 5). For inorganic F^-, adsorption is primarily governed by surface O–H groups and oxygen vacancies, as demonstrated by the attenuation of O–H bands in FT-IR, the reduction of Ce(III)/O_V contents in XPS, and the pronounced decline in removal efficiency following calcination-induced depletion of O–H and O_V sites. In contrast, PFOA adsorption is dominated by interactions with unsaturated Ce(IV) Lewis acid sites, as evidenced by the increase of Ce(III)/O_V after adsorption, the significant suppression of uptake upon PO_4^{3-} addition, and pyridine-IR confirmation of abundant Lewis acid sites. These findings are consistent with literature reports highlighting the abundance of Lewis acid sites on CeO_2 and their ability to polarize and activate C–F bonds [64, 65].

3.4 Theoretical insights into facet-dependent adsorption

To rationalize the facet-dependent adsorption of both inorganic F^- and organic PFOA on CeO_2, DFT calculations were conducted. The formation energies of surface O–H groups were evaluated on the (111), (110), and (100) facets, both with and without O_V (Fig. 6(a) and Fig. S18 in the ESM). The (110) facet exhibited the most favorable O–H formation energy under both conditions, with values of −2.17 eV (without O_V) and −2.45 eV (with O_V), which are notably lower than those of the (100) facet (−1.18 and −1.80 eV) and the (111) facet (−1.21 and −1.76 eV). These results indicate that the (110) facet possesses the highest propensity for hydroxylation, further enhanced by oxygen vacancies, thereby generating a greater density of surface-active O–H sites.

F^- adsorption on the bare CeO_2 surface followed a similar facet-dependent trend (Fig. 6(b) and Fig. S19 in the ESM), with the (110) facet exhibiting the highest affinity and the most favorable adsorption energy, both in the presence and absence of O_V. To further evaluate the ligand-exchange reaction, in which a surface hydroxyl group is replaced by F^-, the free energy changes of F^- adsorption on hydroxylated CeO_2 facets were calculated (Fig. 6(c) and Fig. S20 in the ESM). This reaction was thermodynamically most favorable on the (110) facet (Fig. 6(c)), with free energies of −1.00 eV (without O_V) and −1.62 eV (with O_V). In comparison, the corresponding values were −0.20 and −0.56 eV for the (100) facet, and −0.94 and −1.33 eV for the (111) facet, respectively. Collectively, these findings demonstrate that the (110) facet, characterized by high oxygen vacancy density and strong affinity toward both O–H and F^-, offers abundant reactive hydroxyl sites that promote efficient F^- adsorption and rapid kinetics.

To further elucidate the facet-dependent PFOA adsorption behavior, DFT calculations were performed to investigate the Lewis acidity of unsaturated Ce(IV) sites on the (111), (110), and (100) facets. The optimal PFOA adsorption geometry was first determined, revealing that a "lie-down" configuration—where the PFOA molecule aligns parallel to the surface—was the most thermodynamically favorable across all facets (Fig. S21 in the ESM). This orientation maximizes the exposure of fluorine atoms to the unsaturated Ce(IV) sites, thereby enhancing surface interactions.

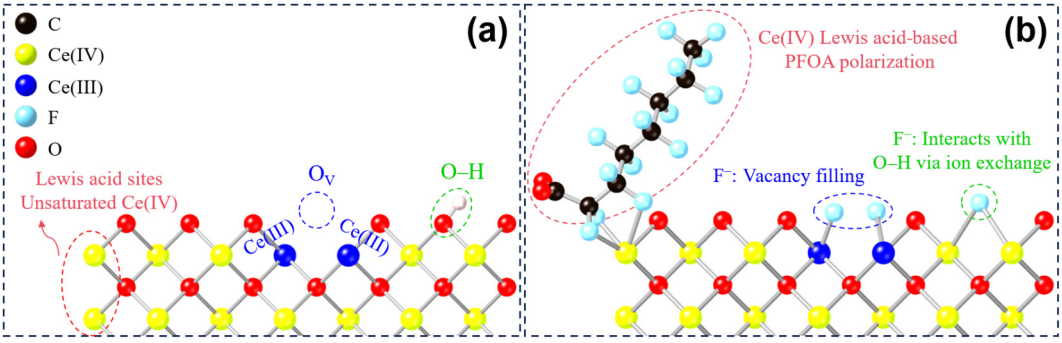

Figure 5 Schematic of the dual active sites of CeO_2 for PFOA and F^- adsorption: CeO_2 surface (a) before and (b) after interaction with PFOA and F^-.

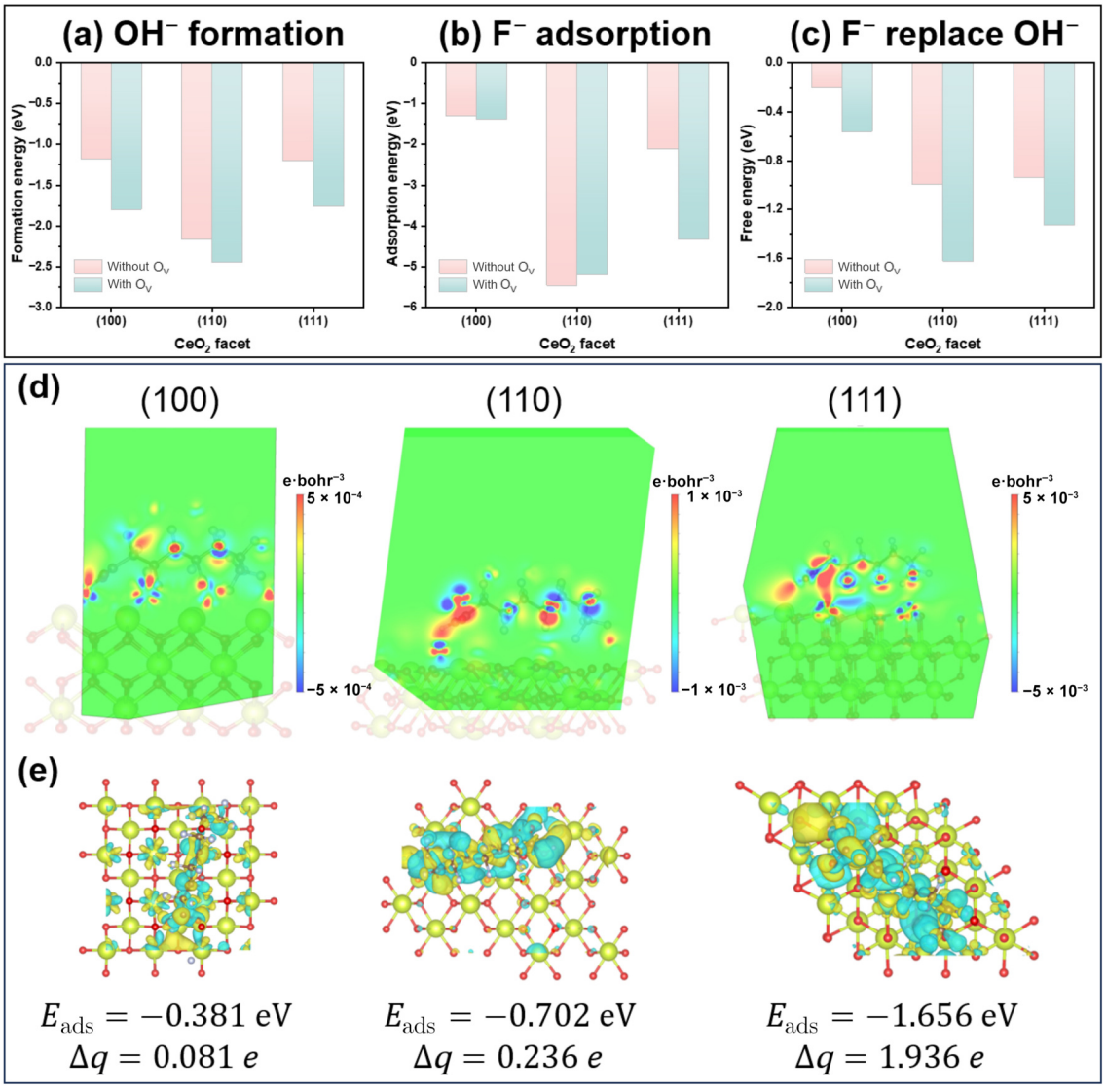

Figure 6 DFT calculations of F^- and PFOA adsorption on different CeO_2 facets: (a) formation energies of surface hydroxyl groups (O–H); (b) F^- adsorption energies on bare CeO_2 surface; (c) free energy change diagram for ligand-exchange reactions where F^- replaces O–H on hydroxyl-covered facets; (d) CDD maps showing electron redistribution between PFOA and Ce(IV) sites (cross-section taken between the nearest F and Ce atoms); and (e) optimized PFOA adsorption configurations and corresponding Bader charge transfer on the (111), (110), and (100) facets (tawny: Ce; red: O; white: H atoms).

Accordingly, this configuration was adopted for all subsequent calculations.

The strength of Lewis acid sites—electron-pair acceptors such as unsaturated Ce(IV)—can be quantitatively assessed via charge density difference (CDD) and Bader charge (BC) analyses in DFT calculations [66, 67]. Stronger Lewis acidity corresponds to greater electron-accepting ability, reflected by more pronounced charge accumulation and larger charge transfer upon adsorption. Accordingly, CDD and BC analyses were conducted to evaluate PFOA adsorption on unsaturated Ce(IV) sites under identical configurations. As shown in Fig. 6(d), the (111) facet exhibited the most significant electron density accumulation between PFOA and Ce(IV), followed by the (110) and (100) facets—consistent with experimental observations. Quantitative analysis (Fig. 6(e)) further revealed that the (111) facet displayed the most favorable adsorption energy (−1.656 eV) and the highest Bader charge transfer (1.936 *e*), compared with the (110) (−0.702 eV, 0.236 *e*) and (100) (−0.381 eV, 0.081 *e*) facets. Collectively, these results confirm that the (111) facet possesses the strongest Lewis acid sites, underpinning its superior PFOA adsorption performance.

4 Conclusions

This study elucidates the facet-dependent dual active-site mechanisms governing CeO_2 interactions with fluorine-bearing contaminants. Facet-controlled CeO_2 nanocrystals exposing dominant (111), (110), and (100) facets were synthesized to distinguish the affinity mechanisms toward PFOA and F^-. The (111)-faceted Oct exhibited the highest capacity and fastest kinetics for PFOA adsorption, while the (110)-faceted Rod showed superior F^- removal. Integrated spectroscopic analyses, quenching tests, and DFT calculations revealed that surface hydroxyl groups and oxygen vacancies dominated F^- adsorption through ion exchange and vacancy filling, whereas unsaturated Ce(IV) Lewis acid sites controlled PFOA adsorption via C–F bond polarization and lattice oxygen substitution. Pyridine-IR quantification and phosphate

inhibition experiments confirmed a direct correlation between Lewis acidity and organic fluorine affinity. DFT results further demonstrated that the (111) facet possesses the strongest Lewis acidity and charge-transfer ability, while the (110) facet favors hydroxylation and fluoride binding. These findings establish a clear structure–facet–function correlation for CeO_2, offering mechanistic insights for the rational design of next-generation fluorine-selective adsorbents and catalytic materials.

Electronic Supplementary Material: Supplementary material (quantitative methods, relevant characterization images and data, analytic models and fitting results, DFT calculation models and results, and relevant adsorption performances) is available in the online version of this article at https://doi.org/10.26599/NR.2026.94908404.

Data availability

All data needed to support the conclusions in the paper are presented in the manuscript and the Electronic Supplementary Material. Additional data related to this paper may be requested from the corresponding author upon request.

Acknowledgements

This work was financially supported by the National Natural Science Foundation of China (No. 22476079), the Key Program of Fundamental Research funded by the Shenzhen Science and Technology Innovation Commission (No. JCYJ20220818100218039), and the Guangdong Major Project of Basic and Applied Basic Research (No. 2023B0303000024). This work was also supported by the State Environmental Protection Key Laboratory of Integrated Surface Water-Groundwater Pollution Control. The authors acknowledge the assistance of SUSTech Core Research Facilities.

Declaration of competing interest

All the contributing authors report no conflict of interests in this work.

Author contribution statement

Y. M. X: Methodology, investigation, conceptualization, data analysis, visualization, writing – original draft. B. Z. C.: Calculation, data analysis, writing – original draft. A. L. W.: Characterization. W. W. C.: Characterization. C. Q. Z.: Characterization; S. D. Z.: Data analysis. Z. P. L.: Data analysis. Z. Y. W.: Conceptualization, funding acquisition, investigation, project administration, resources, writing – review & edit.

Use of AI statement

None.

References

[1] Deng, Z. N.; Xu, A.; Zhang, X. L.; Zhang, K. S.; Pan, B. C. Effects of chelators on fluoride removal by $AlCl_3$ and Al_{13} coagulation: Performance and mechanism. *Environ. Sci. Technol.* **2025**, *59*, 3297–3308.

[2] Deng, Z. N.; Cheng, S. K.; Xu, N.; Zhang, X. L.; Pan, B. C. Pilot-scale field demonstration of environmental nanotechnology for groundwater defluoridation. *ACS EST Eng.* **2023**, *3*, 226–235.

[3] Liang, Z. A.; Lu, Y. L.; Cao, Z. W.; Huang, X. Y.; Lei, H. J.; Li, J. L.; Wu, Z. Y.; An, X. P.; Wang, P. Co-emissions of fluoride ion, fluorinated greenhouse gases, and per- and polyfluoroalkyl substances (PFAS) from different fluorochemical production processes. *Environ. Pollut.* **2024**, *360*, 124609.

[4] The U-turn on PFAS. *Nat. Water* **2023**, *1*, 993–993.

[5] Dhore, R.; Murthy, G. S. Per/polyfluoroalkyl substances production, applications and environmental impacts. *Bioresour. Technol.* **2021**, *341*, 125808.

[6] Zhang, Y.; Wei, C. L.; Song, X.; Tang, Z. W.; Li, Y. L.; Zhang, M. Rapid and effective removal of PFOS from water using ultrathin MgAl-LDH nanosheets with defects. *Chem. Eng. J.* **2025**, *505*, 158998.

[7] Chen, Z. H.; Li, C.; Gao, J.; Dong, H. L.; Chen, Y.; Wu, B.; Gu, C. Efficient reductive destruction of perfluoroalkyl substances under self-assembled micelle confinement. *Environ. Sci. Technol.* **2020**, *54*, 5178–5185.

[8] The PFAS treatment evolution. *Nat. Water* **2025**, *3*, 633–633.

[9] Mariappan Santhi, V.; Periasamy, D.; Perumal, M.; Sekar, P. M.; Varatharajan, V.; Aravind, D.; Senthilkumar, K.; Kumaran, S. T.; Ali, S.; Sankar, S. et al. The global challenge of fluoride contamination: A comprehensive review of removal processes and implications for human health and ecosystems. *Sustainability* **2024**, *16*, 11056.

[10] Franke, V.; Ullberg, M.; McCleaf, P.; Wålinder, M.; Köhler, S. J.; Ahrens, L. The price of really clean water: Combining nanofiltration with granular activated carbon and anion exchange resins for the removal of per- and polyfluoroalkyl substances (PFASs) in drinking water production. *ACS EST Water* **2021**, *1*, 782–795.

[11] Park, M.; Wu, S. M.; Lopez, I. J.; Chang, J. Y.; Karanfil, T.; Snyder, S. A. Adsorption of perfluoroalkyl substances (PFAS) in groundwater by granular activated carbons: Roles of hydrophobicity of PFAS and carbon characteristics. *Water Res.* **2020**, *170*, 115364.

[12] Gar Alalm, M.; Boffito, D. C. Mechanisms and pathways of PFAS degradation by advanced oxidation and reduction processes: A critical review. *Chem. Eng. J.* **2022**, *450*, 138352.

[13] Wilsey, M. K.; Taseska, T.; Meng, Z. Y.; Yu, W. Q.; Müller, A. M. Advanced electrocatalytic redox processes for environmental remediation of halogenated organic water pollutants. *Chem. Commun.* **2023**, *59*, 11895–11922.

[14] Wang, Y. Y.; Pierce, R. D. Jr. ; Shi, H. H.; Li, C. G.; Huang, Q. G. Electrochemical degradation of perfluoroalkyl acids by titanium suboxide anodes. *Environ. Sci.: Water Res. Technol.* **2020**, *6*, 144–152.

[15] Lin, H.; Xiao, R. L.; Xie, R. Z.; Yang, L. H.; Tang, C. M.; Wang, R. R.; Chen, J.; Lv, S. H.; Huang, Q. G. Defect engineering on a Ti_4O_7 electrode by Ce^{3+} doping for the efficient electrooxidation of perfluorooctanesulfonate. *Environ. Sci. Technol.* **2021**, *55*, 2597–2607.

[16] Singh, R. K.; Fernando, S.; Baygi, S. F.; Multari, N.; Thagard, S. M.; Holsen, T. M. Breakdown products from perfluorinated alkyl substances (PFAS) degradation in a plasma-based water treatment process. *Environ. Sci. Technol.* **2019**, *53*, 2731–2738.

[17] Singh, R. K.; Brown, E.; Mededovic Thagard, S.; Holsen, T. M. Treatment of PFAS-containing landfill leachate using an enhanced contact plasma reactor. *J. Hazard. Mater.* **2021**, *408*, 124452.

[18] Isowamwen, O.; Li, R.; Holsen, T.; Thagard, S. M. Plasma-assisted degradation of a short-chain perfluoroalkyl substance (PFAS): Perfluorobutane sulfonate (PFBS). *J. Hazard. Mater.* **2023**, *456*, 131691.

[19] Sharma, S.; Shetti, N. P.; Basu, S.; Nadagouda, M. N.; Aminabhavi, T. M. Remediation of per- and polyfluoroalkyls (PFAS) via electrochemical methods. *Chem. Eng. J.* **2022**, *430*, 132895.

[20] Tshangana, C. S.; Nhlengethwa, S. T.; Glass, S.; Denison, S.;

Kuvarega, A. T.; Nkambule, T. T. I.; Mamba, B. B.; Alvarez, P. J. J.; Muleja, A. A. Technology status to treat PFAS-contaminated water and limiting factors for their effective full-scale application. *npj Clean Water* **2025**, *8*, 41.

[21] Ahrens, T.; Kohlmann, J.; Ahrens, M.; Braun, T. Functionalization of fluorinated molecules by transition-metal-mediated C–F bond activation to access fluorinated building blocks. *Chem. Rev.* **2015**, *115*, 931–972.

[22] Yu, K.; Lou, L. L.; Liu, S. X.; Zhou, W. Z. Asymmetric oxygen vacancies: The intrinsic redox active sites in metal oxide catalysts. *Adv. Sci.* **2020**, *7*, 1901970.

[23] Williams, U. J.; Robinson, J. R.; Lewis, A. J.; Carroll, P. J.; Walsh, P. J.; Schelter, E. J. Synthesis, bonding, and reactivity of a cerium(IV) fluoride complex. *Inorg. Chem.* **2014**, *53*, 27–29.

[24] Liu, X. H.; Xie, L. B.; Liu, Y. G.; Zhao, P.; Han, Y. G.; Cheng, S. S.; Bai, X. Y.; Li, Y. Rapid preparation of highly stable ZnO-CeO_2/CF cathode by one-step electro-deposition for efficient degradation of ciprofloxacin in electro-Fenton system. *Catal. Today* **2020**, *355*, 458–465.

[25] Wang, J.; Xu, W. H.; Chen, L.; Jia, Y.; Wang, L.; Huang, X. J.; Liu, J. H. Excellent fluoride removal performance by CeO_2-ZrO_2 nanocages in water environment. *Chem. Eng. J.* **2013**, *231*, 198–205.

[26] Choong, C. E.; Kim, M.; Lim, J. S.; Hong, Y. J.; Lee, G. J.; Chae, K. H.; Nah, I. W.; Yoon, Y.; Choi, E. H.; Jang, M. Understanding the synergistic effect of hydrated electron generation from argon plasma catalysis over Bi_2O_3/CeO_2 for perfluorooctanoic acid dehalogenation: Mechanism and DFT study. *Appl. Catal. B: Environ.* **2024**, *343*, 123403.

[27] Cao, S. H.; Yang, H. C.; Cheng, C.; Dai, J. H.; Lu, S. S.; Lu, Y. *In-situ* synthesis of Z-scheme CeO_2@WO_3 heterojunction with aromatic rings as electron medium for efficient photocatalytic degradation of perfluorobutane sulfonate. *J. Rare Earths* **2025**, *43*, 470–479.

[28] Liu, X.; Shu, Y. F.; Pan, Y.; Zeng, G. S.; Zhang, M.; Zhu, C. Q.; Xu, Y. M.; Wan, A. L.; Wang, M. X.; Han, Q. et al. Electrochemical destruction of PFAS at low oxidation potential enabled by CeO_2 electrodes utilizing adsorption and activation strategies. *J. Hazard. Mater.* **2025**, *486*, 137043.

[29] Wang, K. T.; Lei, H. Y.; Muhammad, Y.; Chen, F.; Gao, F.; Wei, Y. Z.; Fujita, T. Controlled preparation of cerium oxide loaded slag-based geopolymer microspheres (CeO_2@SGMs) for the adsorptive removal and solidification of F^- from acidic waste-water. *J. Hazard. Mater.* **2020**, *400*, 123199.

[30] Wang, Y. J.; Luo, X. G. Efficient adsorptive removal of low concentration fluoride ions from water by cellulose beads with trapped CeO_2 nanoparticles. *J. Environ. Chem. Eng.* **2024**, *12*, 113180.

[31] Zhang, C. M.; Liang, L.; Zhao, S. L.; Wu, Z. J.; Wang, S. H.; Yin, D. M.; Wang, Q. S.; Wang, L. M.; Wang, C. L.; Cheng, Y. Dehydrogenation behavior and mechanism of $LiAlH_4$ adding nano-CeO_2 with different morphologies. *Nano Res.* **2023**, *16*, 9426–9434.

[32] Shi, Q. Q.; Zhang, Y. F.; Li, Z. W.; Han, Z. K.; Xu, L. L.; Baiker, A.; Li, G. Morphology effects in $MnCeO_x$ solid solution-catalyzed NO reduction with CO: Active sites, water tolerance, and reaction pathway. *Nano Res.* **2023**, *16*, 6951–6959.

[33] Chen, W. S.; Xue, J.; Bao, Y. F.; Feng, L. G. Surface engineering of Nano-ceria facet dependent coupling effect on Pt nanocrystals for electro-catalysis of methanol oxidation reaction. *Chem. Eng. J.* **2020**, *381*, 122752.

[34] Tan, Z. C.; Wu, T. S.; Soo, Y. L.; Peng, Y. K. Unravelling the true active site for CeO_2-catalyzed dephosphorylation. *Appl. Catal. B: Environ.* **2020**, *264*, 118508.

[35] Shao, J.; Wang, J. H.; Zhang, Y. F.; Xue, S. Z.; Dong, H.; Liu, H. C.; Li, C.; Zhang, Y. W. Amino acid electrosynthesis with oxygen vacancy-mediated CeO_2 nanocrystals: Facet effect and catalytic mechanism. *JACS Au* **2025**, *5*, 2015–2026.

[36] Tan, H. Y.; Wang, J.; Yu, S. Z.; Zhou, K. B. Support morphology-dependent catalytic activity of Pd/CeO_2 for formaldehyde oxidation. *Environ. Sci. Technol.* **2015**, *49*, 8675–8682.

[37] Pan, H.; Chen, Z. H.; Feng, X. B.; Cao, S. J.; Jian, Y. F.; Chen, J.; He, C. Sulfur-resistant mechanism of MnO_x@CeO_2@MgO core–shell catalyst in simultaneous removal of NO_x and chlorobenzene. *Appl. Catal. B: Environ. Energy* **2025**, *362*, 124761.

[38] Kresse, G.; Furthmüller, J. Efficiency of *Ab-initio* total energy calculations for metals and semiconductors using a plane-wave basis set. *Comput. Mater. Sci.* **1996**, *6*, 15–50.

[39] Liu, J. C.; Wang, Y. G.; Li, J. Toward rational design of oxide-supported single-atom catalysts: Atomic dispersion of gold on ceria. *J. Am. Chem. Soc.* **2017**, *139*, 6190–6199.

[40] Capdevila-Cortada, M.; Łodziana, Z.; López, N. Performance of DFT+U approaches in the study of catalytic materials. *ACS Catal.* **2016**, *6*, 8370–8379.

[41] Grimme, S.; Antony, J.; Ehrlich, S.; Krieg, H. A consistent and accurate *ab initio* parametrization of density functional dispersion correction (DFT-D) for the 94 elements H–Pu. *J. Chem. Phys.* **2010**, *132*, 154104.

[42] Momma, K.; Izumi, F. *VESTA 3* for three-dimensional visualization of crystal, volumetric and morphology data. *J. Appl. Cryst.* **2011**, *44*, 1272–1276.

[43] Zhu, Y. Z.; Chen, C. G.; Cheng, P.; Ma, J.; Yang, W. B.; Yang, W. X.; Peng, Y. R.; Huang, Y. G.; Zhang, S. P.; Seong, G. Recent advances in hydrothermal synthesis of facet-controlled CeO_2-based nanomaterials. *Dalton Trans.* **2022**, *51*, 6506–6518.

[44] Chen, F.; Shen, X. X.; Wang, Y. C.; Zhang, J. L. CeO_2/H_2O_2 system catalytic oxidation mechanism study via a kinetics investigation to the degradation of acid orange 7. *Appl. Catal. B: Environ*. **2012**, *121–122*, 223–229.

[45] Song, B. C.; Si, S. X.; Soleymani, A.; Xin, Y.; Hagelin-Weaver, H. E. Effect of ceria surface facet on stability and reactivity of isolated platinum atoms. *Nano Res.* **2022**, *15*, 5922–5932.

[46] Mullins, D. R. The surface chemistry of cerium oxide. *Surf. Sci. Rep.* **2015**, *70*, 42–85.

[47] Zhang, B. L.; Yang, Z. H.; Yan, C. Y.; Xue, Z. M.; Mu, T. C. Operando forming of lattice vacancy defect in ultrathin crumpled NiVW-layered metal hydroxides nanosheets for valorization of biomass. *Small* **2023**, *19*, 2207236.

[48] Zhang, Y.; Lu, J. C.; Zhang, L. M.; Fu, T.; Zhang, J.; Zhu, X.; Gao, X. Y.; He, D. D.; Luo, Y. M.; Dionysiou, D. D. et al. Investigation into the catalytic roles of oxygen vacancies during gaseous styrene degradation process via CeO_2 catalysts with four different morphologies. *Appl. Catal. B: Environ.* **2022**, *309*, 121249.

[49] Loridant, S. Raman spectroscopy as a powerful tool to characterize ceria-based catalysts. *Catal. Today* **2021**, *373*, 98–111.

[50] Wu, C. Y.; Klemes, M. J.; Trang, B.; Dichtel, W. R.; Helbling, D. E. Exploring the factors that influence the adsorption of anionic PFAS on conventional and emerging adsorbents in aquatic matrices. *Water Res.* **2020**, *182*, 115950.

[51] Austin, C.; Purohit, A. L.; Thomsen, C.; Pinkard, B. R.; Strathmann, T. J.; Novosselov, I. V. Hydrothermal destruction and defluorination of Trifluoroacetic acid (TFA). *Environ. Sci. Technol.* **2024**, *58*, 8076–8085.

[52] Zhou, J. Y.; Saeidi, N.; Wick, L. Y.; Xie, Y. L.; Kopinke, F. D.; Georgi, A. Efficient removal of Trifluoroacetic acid from water using surface-modified activated carbon and electro-assisted desorption. *J. Hazard. Mater.* **2022**, *436*, 129051.

[53] Mohona, T. M.; Ye, Z. J.; Dai, N.; Nalam, P. C. Adsorption behavior of long-chain perfluoroalkyl substances on hydrophobic surface: A combined molecular characterization and simulation study. *Water Res.* **2023**, *239*, 120074.

[54] Pan, Y.; Liu, X.; Zhang, M.; Han, Q.; Shu, Y. F.; Wang, M. X.; Liu, B.; Wang, Z. Y. The impact of redox annealing on intrinsic properties and fluoride adsorption performance of CeO_2 nanomaterials. *Chem. Eng. J.* **2023**, *476*, 146347.

[55] Zang, L. L.; Zhu, C. Q.; Zhang, M.; Shu, Y. F.; Liu, X.; Wang, Z. Y. Comparative analysis of enhanced adsorption and thermal decomposition of oil-borne PFAS using CeO_2 nanoparticles and activated carbon. *J. Hazard. Mater. Adv.* **2024**, *16*, 100469.

[56] Tan, Z. C.; Zhang, J. R.; Chen, Y. C.; Chou, J. P.; Peng, Y. K. Unravelling the role of structural geometry and chemical state of well-defined oxygen vacancies on pristine CeO_2 for H_2O_2 activation. *J. Phys. Chem. Lett.* **2020**, *11*, 5390–5396.

[57] Kang, D. J.; Yu, X. L.; Ge, M. F. Morphology-dependent properties and adsorption performance of CeO_2 for fluoride removal. *Chem. Eng. J.* **2017**, *330*, 36–43.

[58] Yang, S. Y.; Zhang, W. S.; Pan, G. L.; Chen, J. Y.; Deng, J. Y.; Chen, K.; Xie, X. L.; Han, D. X.; Dai, M. J.; Niu, L. Photocatalytic co-reduction of N_2 and CO_2 with CeO_2 catalyst for urea synthesis. *Angew. Chem., Int. Ed.* **2023**, *62*, e202312076.

[59] Hou, B.; Pan, J. W.; Shi, T.; Dang, Z. H.; Yang, S.; Wang, L.; Gao, B. Y. Efficient removal of hexavalent chromium by nano-cerium-based adsorbent: The critical role of valence state and oxygen vacancy. *J. Hazard. Mater.* **2024**, *464*, 133020.

[60] Yang, M.; Shen, G. L.; Wang, Q.; Deng, K.; Liu, M.; Chen, Y. F.; Gong, Y.; Wang, Z. Roles of oxygen vacancies of CeO_2 and Mn-doped CeO_2 with the same morphology in benzene catalytic oxidation. *Molecules* **2021**, *26*, 6363.

[61] Jing, R.; Lu, X. B.; Wang, J. F.; Xiong, J.; Qiao, Y. N.; Zhang, R.; Yu, Z. H. CeO_2-based frustrated Lewis pairs via defective engineering: Formation theory, site characterization, and small molecule activation. *Small* **2024**, *20*, 2310926.

[62] Wang, Y. X.; Chen, L. L.; Cao, H. B.; Chi, Z. X.; Chen, C. M.; Duan, X. G.; Xie, Y. B.; Qi, F.; Song, W. Y.; Liu, J. et al. Role of oxygen vacancies and Mn sites in hierarchical Mn_2O_3/$LaMnO_{3-\delta}$ perovskite composites for aqueous organic pollutants decontamination. *Appl. Catal. B: Environ.* **2019**, *245*, 546–554.

[63] Wu, L. Y.; Wang, Z. L.; Liu, J. Y.; Liu, C. H.; Li, X. Y.; Zhang, Y. X.; Wang, W.; Ma, J.; Sun, Z. Q. Selective ozone catalyzation modulated by surface and bulk oxygen vacancies over MnO_2 for superior water purification. *Appl. Catal. B: Environ.* **2024**, *343*, 123526.

[64] Chen, Y. K.; Qu, W. Q.; Luo, T.; Zhang, H.; Fu, J. W.; Li, H. M.; Liu, C. X.; Zhang, D. S.; Liu, M. Promoting C–F bond activation via proton donor for CF_4 decomposition. *Proc. Natl. Acad. Sci. USA* **2023**, *120*, e2312480120.

[65] Stahl, T.; Klare, H. F. T.; Oestreich, M. Main-group Lewis acids for C–F bond activation. *ACS Catal.* **2013**, *3*, 1578–1587.

[66] Chen, B. F.; Duan, Y. Y.; Gong, H. F.; Du, Z. R. H.; Li, S. J.; Li, Y. H.; Wang, Q.; Ye, Z. J.; Zhang, D. Q. Acid sites cleavage of surface-frustrated Lewis pairs for small-molecule activation of mixed volatile pollutants. *Environ. Sci. Technol.* **2025**, *59*, 11686–11697.

[67] Choi, C.; Wang, X. X.; Kwon, S.; Hart, J. L.; Rooney, C. L.; Harmon, N. J.; Sam, Q. P.; Cha, J. J.; Goddard, W. A.; Elimelech, M. et al. Efficient electrocatalytic valorization of chlorinated organic water pollutant to ethylene. *Nat. Nanotechnol.* **2023**, *18*, 160–167.